Icarus 246 (2015) 11–20

Contents lists available at ScienceDirect

Icarus

journal homepage: www.elsevier.com/locate/icarus

The interior and orbital evolution of Charon as preserved in its geologic record

Alyssa Rose Rhoden [a,*,1], Wade Henning [a,b], Terry A. Hurford [a], Douglas P. Hamilton [b]

[a] NASA Goddard Space Flight Center, Code 693, Greenbelt, MD 20771, United States
[b] Department of Astronomy, University of Maryland, College Park, College Park, MD 20742, United States

ARTICLE INFO

Article history:
Received 28 December 2013
Revised 18 April 2014
Accepted 18 April 2014
Available online 30 April 2014

Keywords:
Charon
Rotational dynamics
Tectonics
Pluto, satellites
Satellites, surfaces

ABSTRACT

Pluto and its largest satellite, Charon, currently orbit in a mutually synchronous state; both bodies continuously show the same face to one another. This orbital configuration is a natural end-state for bodies that have undergone tidal dissipation. In order to achieve this state, both bodies would have experienced tidal heating and stress, with the extent of tidal activity controlled by the orbital evolution of Pluto and Charon and by the interior structure and rheology of each body. As the secondary, Charon would have experienced a larger tidal response than Pluto, which may have manifested as observable tectonism. Unfortunately, there are few constraints on the interiors of Pluto and Charon. In addition, the pathway by which Charon came to occupy its present orbital state is uncertain. If Charon's orbit experienced a high-eccentricity phase, as suggested by some orbital evolution models, tidal effects would have likely been more significant. Therefore, we determine the conditions under which Charon could have experienced tidally-driven geologic activity and the extent to which upcoming New Horizons spacecraft observations could be used to constrain Charon's internal structure and orbital evolution. Using plausible interior structure models that include an ocean layer, we find that tidally-driven tensile fractures would likely have formed on Charon if its eccentricity were on the order of 0.01, especially if Charon were orbiting closer to Pluto than at present. Such fractures could display a variety of azimuths near the equator and near the poles, with the range of azimuths in a given region dependent on longitude; east–west-trending fractures should dominate at mid-latitudes. The fracture patterns we predict indicate that Charon's surface geology could provide constraints on the thickness and viscosity of Charon's ice shell at the time of fracture formation.

1. Introduction

Pluto and its largest moon, Charon, presently occupy a mutually synchronous state, with a period of 6.387 days (e.g. Buie et al., 2012). Along with Charon's zero eccentricity (Buie et al., 2012), this dynamical relationship means that Charon likely experiences very limited tidal deformation because the relative position and distance to Pluto remains the same throughout each orbit. Hence, we would not expect to find recent tidally-driven tectonics or active jets such as those observed at Enceladus (e.g. Spencer et al., 2006; Porco et al., 2006) and possibly Europa (Roth et al., 2013). However, past conditions may have allowed for extensive tidal activity.

Most models of Charon's formation allow for the possibility that Charon initially orbited much closer to Pluto than at present, that it experienced a transient high eccentricity phase, and that Charon was heated to the point of differentiation (e.g. Ward and Canup, 2006; Cheng et al., 2014). Such conditions make it plausible that, at some point in its evolution, Charon had an ice shell overlying a liquid water or brine ocean, which could have been quite responsive to tidal stress. If Charon experienced a high eccentricity phase concurrent with the existence of an ocean layer, tidally-driven fracturing may have been possible, similar to that observed at Europa (e.g. Greenberg et al., 1998). However, as with Europa, the magnitude of the tidal stress would depend on the thickness and rheology of Charon's internal layers (Wahr et al., 2009; Jara-Orué and Vermeersen, 2011) as well as its eccentricity and orbital distance. Therefore, the goals of this work are to quantify the conditions under which Charon could have achieved tidal stresses comparable to those on other icy ocean worlds, to predict the extent and character of tidally-driven fracturing under those

* Corresponding author.
E-mail address: Alyssa.R.Rhoden@nasa.gov (A.R. Rhoden).
[1] Previously published under the surname Sarid.

http://dx.doi.org/10.1016/j.icarus.2014.04.030
0019-1035/

conditions, and to determine whether Charon's tectonic record could be used to constrain the evolution of its interior and orbit.

In Section 2, we provide an overview of tidal-tectonic processes on icy bodies, hypotheses for Charon's formation and evolution, and constraints on Charon's interior and composition. In Section 3, we present our methods for calculating tidally-induced surface stresses for a multilayer viscoelastic body with a liquid ocean and for generating fracture predictions based on tidal stress. We also discuss our test cases, in which we vary the thickness of the hypothesized ice shell, the thickness of the brittle and ductile layers within the shell, and the viscosity of the lower, ductile ice layer. Results are presented and discussed in Section 4. We find that tidally-driven fractures would likely have formed on Charon, using plausible interior structure models that include an ocean layer, in response to an eccentricity of order 0.01, especially if the increased eccentricity occurred when Charon orbited closer to Pluto than at present. Furthermore, our predictions of fracture locations and azimuths indicate that Charon's surface fractures, or lack thereof, can provide constraints on the thickness and viscosity of Charon's ice shell at the time of fracture formation.

In 2015, the New Horizons spacecraft is expected to arrive at Pluto and begin collecting a wealth of data on Pluto and its companion moons (e.g., Stern and Spencer, 2003; Young et al., 2008; Fountain et al., 2009). At a minimum, New Horizons plans to image one hemisphere of Charon, at 500 m/pixel resolution, which should be sufficient to characterize its geology (Young et al., 2008). Additional higher-resolution targeted images are also planned. Hence, the data set obtained by New Horizons should enable identification of tidally-driven fractures through comparison with the predictions provided herein.

2. Background

2.1. Tidal-tectonics on icy bodies

Because Charon may have had both an ice-covered ocean and a high eccentricity it its past, it is useful to review tidal-tectonic processes on other icy ocean moons in our Solar System. Jupiter's moon, Europa, participates in mean-motion resonances with neighboring moons, Io and Ganymede, which force its orbit to remain eccentric (e.g. Peale, 1999; Greenberg et al., 1998). In addition, magnetometer observations indicate that Europa's outer ice shell overlies a thick, liquid water ocean (Anderson et al., 1998), which has likely persisted due to tidal heating. The ocean's response to Jupiter's diurnally-varying gravitational pull generates stress in the overlying ice shell, likely fracturing the icy surface. In fact, many observed tectonic features have been linked to tensile fractures predicted to occur as a result of tidal stress due to eccentricity, obliquity, and spin pole precession (e.g. Kattenhorn and Hurford, 2009; Rhoden et al., 2010; Rhoden and Hurford, 2013). The role of non-synchronous rotation in forming fractures has also been considered (Helfenstein and Parmentier, 1983, 1985; Geissler et al., 1998; Greenberg et al., 1998; Figueredo and Greeley, 2000; Kattenhorn, 2002; Sarid et al., 2004, 2005, 2006; Groenleer and Kattenhorn, 2008), although more recent work suggests that non-synchronous rotation stress is unlikely to significantly affect the orientations of tidally-driven fractures (Goldreich and Mitchell, 2010; Rhoden et al., 2010, 2012; Rhoden and Hurford, 2013). Earth-based radar measurements have confirmed that Europa's present day obliquity is non-zero (Margot et al., 2013), consistent with interpretations of the tectonic record. In addition, time-variable UV emission from Europa's south pole has been interpreted as a water plume, which suggests that tidally-driven processes may still be active today (Roth et al., 2013).

The global patterns of Europa's lineaments and cycloids, along with detailed cycloid fits, correlate very well with tidal stress predictions, but imply that the ice shell fails under rather low stresses (Hoppa et al., 2001; Hurford et al., 2007b; Rhoden et al., 2010; Rhoden and Hurford, 2013). Good fits to six observed cycloids each correspond to a different "best fit" failure stress, ranging from 49 kPa to 94 kPa (Rhoden et al., 2010). Fits to lineament azimuth patterns suggest failure as low as 20 kPa (Rhoden and Hurford, 2013). In contrast, laboratory measurements show that the failure strength of pure water ice is ~1 MPa (Schulson, 2001); colder temperatures further increase the tensile strength in lab studies (Litwin et al., 2012). However, additional isotropic stresses from cooling and thickening of the ice shell could provide enough stress to crack the ice and amplify the signal of tidal stress (Nimmo, 2004). This process may have also been relevant for Charon if its interior was initially warm.

Enceladus, a small moon of Saturn, also participates in a mean motion resonance, maintains a forced eccentricity, and has a young surface that displays a rich history of tectonic activity. In addition, the Cassini spacecraft detected plumes emanating from several fractures located near Enceladus' south pole, demonstrating that the moon is currently, and dramatically, geologically active (Spencer et al., 2006; Porco et al., 2006). Variability in the timing of plume eruptions is consistent with the hypothesis that changes in tidal stress control the behavior of the fractures, leading to eruptions (Hurford et al., 2007a, 2012; Hedman et al., 2013). Several lines of evidence support the existence of a liquid water reservoir at Enceladus' south pole, including models of plume formation (e.g. Collins and Goodman, 2007), interpretations of gravity data (Iess et al., 2014), and thermal evolution models of Enceldaus' interior showing that a global ocean is challenging to maintain (Roberts and Nimmo, 2008; Tobie et al., 2008; Behounková et al., 2012). In contrast, analysis of Enceladus' tectonic record suggests the presence of a global ocean (Patthoff and Kattenhorn, 2011), rather than a regional sea, at least at some time in Enceladus' recent past. Most calculations of tidal stress on icy satellites have relied on the assumption that the ice shell behaves elastically and neglected any effects of the internal structure or rheology of the satellite's interior (e.g. Greenberg et al., 1998; Nimmo et al., 2007). However, tools have since been developed to calculate tidal stress in a viscoelastic ice shell and for a variety of layered interior structures (Wahr et al., 2009; Jara-Orué and Vermeersen, 2011). Although tidal-tectonic models using the simplified approach have provided good fits to observed features on Europa (e.g. Rhoden et al., 2010), accounting for the interior structure and rheology does change the pattern of tidal stress and the resulting predictions of fracture formation (Jara-Orué and Vermeersen, 2011; Rhoden et al., 2013). And, for bodies with thicker or warmer ice shells, the viscoelastic approach is certainly more appropriate. Although the current orbital configuration of Pluto and Charon makes eccentricity-driven tidal deformation unlikely, past conditions may have allowed for the formation of at least some tidally-driven fractures.

2.2. Charon formation models and observations

The leading theory for the formation of Charon is that it accreted from debris lofted into orbit by a giant impact on Pluto (e.g., McKinnon, 1989; Canup, 2005; Stern et al., 2006). In that case, Charon would have rapidly agglomerated (on a timescale of months) from a disk of material in a very close, circular, and uninclined orbit. In a few tens of thousands of years, tidal torques from Pluto would have slowed Charon's spin rate until it became synchronously locked to Pluto (Peale, 1999). Then, in a much slower process (i.e. millions of years), tidal torques exerted by Charon on Pluto would have reduced Pluto's spin rate while expanding Charon's orbit. The increase in Charon's distance from Pluto would reduce the magnitude of its tidal bulges, perhaps leading to fracturing (e.g. Barr and Collins, 2013). If Charon's orbit remained circular

throughout its orbital recession, the only expected source of tidally-driven fractures would be the slow collapse of Charon's tidal bulges, which would result in mainly east–west oriented faults, concentrated at the leading and trailing apexes (e.g. Fig. 12b of Kattenhorn and Hurford, 2009). The sub-Pluto and anti-Pluto points would experience compression throughout the orbit, and thus, no tensile fractures would be expected to form there.

However, some models of Charon's orbital evolution permit the possibility that Charon experienced a transient high eccentricity phase as its orbit expanded (e.g. Ward and Canup, 2006; Cheng et al., 2014). During orbital evolution, there are competing effects: tides raised by Charon on Pluto, which act to increase Charon's orbital eccentricity, and tides raised by Pluto on Charon, which damp Charon's eccentricity. Typically, the tides raised by a planet on its satellite will dominate, but Charon's large size relative to Pluto (~1/8th by mass) makes the orbital evolution more complex, perhaps including a period of high eccentricity. Ultimately, as synchronous orbit is approached, tides raised on Pluto must diminish in importance and Charon's orbit must circularize. Whether this high eccentricity phase would have produced more extensive tectonism, such as observed on Europa and Enceladus, depends on several factors, including: (a) the magnitude of the eccentricity, (b) Charon's orbital distance during the high-eccentricity phase, (c) the presence of a liquid water ocean, (d) the thickness of the ice shell, (e) the viscosity of the ice shell, and (f) the strength of the ice shell. Hence, the presence or absence of fractures on Charon will provide constraints on its orbital and interior evolution.

Predicting Charon's interior structure is largely dependent on the formation scenario one assumes. In the giant impact model, Charon would have formed hot, leading to rapid differentiation and the development of an ice shell overlying a liquid water ocean. In addition, a giant impact or glancing impact onto Pluto, as well as formation via dynamical capture (Piros dos Santos et al., 2012), would imply a dynamically excited initial state, which could also generate heat to drive differentiation. In any case, as Charon cooled, and its dynamical state evolved toward a circular, synchronous orbit, the ice shell may have thickened, freezing out the ocean underneath (Desch et al., 2009). Only the in situ gravitational collapse model of the binary planet system (Nesvorný et al., 2010) would imply a cool and dynamically relaxed origin for Charon, most likely resulting in an undifferentiated interior.

At present, there is only weak observational evidence for past activity on Charon. Charon's radius has been inferred from stellar occultations (Null et al., 1993; Lee and Peale, 2006; Sicardy et al., 2006), to be 603.6 ± 1.4 km. Combined with mass estimates, the corresponding density would be1710 ± 0.08 kg m^{-3}. Spectroscopic observations during an occultation of Pluto and Charon revealed the interesting fact that Charon's surface is dominated by water ice (Buie et al., 1997, 2006; Buie and Grundy, 2000; Cook et al., 2007; Cruikshank et al., 1997; Brown, 2002; Protopapa et al., 2008), whereas Pluto's surface is mainly N_2/CH_4. In addition, and perhaps more importantly, the spectra indicate the presence of crystalline ice (e.g. Brown and Calvin, 2000), which has been interpreted as evidence for recent cryovolcanism. Evidence for crystalline ice strongly suggests that Charon may have had sufficient internal heating for an ice shell to remain decoupled from a solid silicate/iron core, and that such a state may even persist to the present day.

3. Methodology

3.1. Predicting fracture formation on Charon

To compute tidal stress on Charon, we follow the formulation of Jara-Orué and Vermeersen (2011), which utilizes the propagator matrix method. Because the equations are solved in the Laplace domain, rather than the Fourier domain (cf. Wahr et al., 2009), the tidal stress calculations require parameters that depend on the internal structure, and must be solved for first. Hence, we describe this approach as a two-step process. First, we determine the tidal response of Charon by calculating the Love numbers and the strengths of normal modes that correspond to interfaces between its internal layers (see Appendix A). The tidal response depends mainly on the thickness and viscosity that we assume for each layer. Second, we use the tidal response parameters as inputs into the tidal stress calculations, which have been derived for a viscoelastic body under both short and long-term forcing (Jara-Orué and Vermeersen, 2011). Finally, we predict the azimuths at which we would expect fractures to form on Charon, for a given interior-rotation model, as distributed on a latitude–longitude grid.

Within a given region, we predict that a fracture would be present in the tectonic record if the tensile stress perpendicular to its azimuth rises above 50 kPa at any point during the orbit. A failure threshold of 50 kPa is consistent with the minimum failure stress indicated by fits to observed cycloids on Europa (e.g. Rhoden et al., 2010), which are the most diagnostic features attributed to tidal stress on that satellite. Our predictions include fractures that would form orthogonal to the most tensile principal stress in the region and fractures that could propagate through the region, with azimuths determined by the stress conditions where they formed. The basis for this approach also comes from analysis of tectonic features on Europa. While the majority of Europa's lineaments have azimuths that are perpendicular to the most tensile principal stress throughout an orbit, the diversity of observed azimuths in a given region requires an additional mechanism, such as fractures that formed elsewhere and propagated through the region (Rhoden and Hurford, 2013).

To determine whether this criterion is met, we first compute the tidal stress tensor at 48, evenly-spaced, time steps throughout an orbit, for a given latitude, longitude, and interior-rotation model. This time resolution is sufficient to identify differences in tidal stress due to the structure and rheology of the interior (Jara-Orué and Vermeersen, 2011). We then decompose the stress tensor into normal and shear stresses for each azimuth, from 0° to 179°, and identify the peak normal tensile stress for each azimuth throughout the orbit. If the peak normal stress is ever larger than 50 kPa, we predict that a fracture could be observed at that azimuth. Because the distribution of stress depends on the interior and orbital parameters we assume, differences in the predicted patterns of tectonic features can serve as diagnostic tests of Charon's internal structure and orbital evolution. In addition to the predicted fracture pattern, for each interior–orbital model, we identify the global peak tensile stress, regardless of fracture location or azimuth. In general, interior models that result in a high global peak tensile stress are correlated with a wider distribution of predicted fractures than those with lower global peak tensile stress.

3.2. Interior structure test cases and dynamical parameters

Using the observed bulk density and radius of Charon as constraints, we compute a self-consistent, 5-layer model of its interior. All of our interior models include an iron core, silicate mantle, and liquid water ocean overlain by an ice shell that is separated into a lower ductile layer and an upper brittle layer. The total thicknesses of the core, mantle, and ice–ocean layers are further constrained by the relative densities we assume for each material. Assuming a differentiated silicate/iron core with an iron/rock fraction of 0.29, results in a 200 km iron core, a 170.5 km silicate mantle, and an ice–ocean combined thickness of 233 km. The resulting ice/rock mass fraction is 1.12.

Table 1
Parameters defining Charon's interior.

Layer	Density (kg m^{-3})	Shear modulus (Pa)	Viscosity (Pa s)	Thickness (km)
Iron core	5500	n/a[a]	n/a[a]	200
Silicate mantle	3500	6.5×10^{10}[d]	1×10^{19}[b,d]	170.5
Water ocean	1000*	0	~0	Constrained by ice thickness[e]
Ductile ice	999*	3.4×10^{9}[c,d]	10^{13}, 10^{14}[c], or 10^{15}	Total ice shell = 15, 30, 60, or 100 km; Brittle layer = 2, 5, or 10 km
Brittle ice	999*	3.4×10^{9}[c,d]	1×10^{21}[c,d]	

* Densities closely, but not exactly, matched in order to simplify mass conservation while avoiding computational instability at the ocean interface.
[a] See Appendix A for core handling.
[b] Henning et al. (2009).
[c] Poirier (1982) and Goldsby and Kohlstedt (2001).
[d] Jara-Orué and Vermeersen (2011).
[e] The total ice–ocean thickness is fixed at 233 km.

Parameters for our interior structure models are listed in Table 1. To investigate the role of layer structure and rheology on Charon's tidal response, we vary the viscosity of the lower ductile ice shell (10^{13} Pa s, 10^{14} Pa s, or 10^{15} Pa s), the thickness of the whole ice layer (15 km, 30 km, 60 km, or 100 km), and the thickness of the brittle upper ice layer (2 km, 5 km, or 10 km). We preserve the total ice–ocean thickness of 233 km in each case. Table 2 lists the parameter values for each of the test cases. Common values for the shear modulus of icy satellites vary by, at most, a factor of two, whereas the uncertainty in viscosity varies by several orders of magnitude. Hence, while both values will contribute to the tidal stresses we calculate, the observed tectonic patterns are much more likely to provide insight into the viscosity of the lower ice shell rather than the shear modulus, which we thus hold constant. Given our limited knowledge of Charon's internal structure and rheology, it is challenging to select parameter values with much confidence, so we instead attempt to explore a wide, but plausible, search space.

Even with an internal structure favorable to large tides, stress will only be induced if Charon's orbit or rotation state changes with time. In the leading formation hypothesis, the giant impact model, it is a near certainty that the satellite once had a shorter orbital period. However, Charon's eccentricity at that time is relatively unconstrained. For example, Cheng et al. (2014) begin their simulations of the mutual orbital evolution of Pluto and Charon with Charon at a distance of only $4R_{\mathrm{Pluto}}$ and with an eccentricity between 0.1 and 0.3. Even late in the evolution, when Charon has evolved to nearly its present orbital distance, the eccentricity can still be >0.1. Hence, the modeling results of Cheng et al. (2014) allow for a wide variety of possible evolution histories.

Here, we test the influence of a high-eccentricity phase by computing stresses using eccentricities of 0.001 and 0.01, and at both the current period of 6.387 days (corresponding to a distance of $\sim 17R_{\mathrm{Pluto}}$) and half that period ($\sim 10R_{\mathrm{Pluto}}$). Tidal stress magnitudes increase linearly with increasing eccentricity, whereas the response of Charon's internal layers depends sensitively (and non-linearly) on the orbital period (Jara-Orué and Vermeersen, 2011). Our choices for eccentricity and period are rather conservative compared to the modeling results of Cheng et al. (2014). We expect that these values are more consistent with the end stages of orbital evolution and, therefore, should yield the youngest tidal fractures preserved in the geologic record. Furthermore, we consider our choices of eccentricity and period to be illustrative only; it is not our intention to assert that Charon experienced exactly these conditions.

4. Results

We find that the minimum eccentricity required to achieve faulting under Europa-like conditions is between 0.001 and 0.01, depending on the period we assume for Charon. An eccentricity of 0.001 does not produce tidal stresses that exceed our 50 kPa failure threshold for any interior structure model that we tested, for either orbital period. In fact, the stresses would not even exceed 20 kPa under these conditions. Increasing the eccentricity to 0.01 still cannot produce fractures at the current period. However, reducing the period by half (corresponding to an orbital distance of $10R_{\mathrm{P}}$) and assuming an eccentricity of 0.01 can produce faulting in many cases. We limit our following discussion, and accompanying figures, to the results using these values. Due to degeneracy between the eccentricity and period, there are likely many combinations that would generate comparable stresses and similar fracture predictions.

The viscosity of the lower, ductile ice shell has the largest influence on the fault predictions. In Fig. 1, we show the change in global peak tensile stress (given in Table 2) with ductile ice viscosity

Table 2
Parameters for each test case.

Case	*Ductile ice viscosity (Pa s)*	*Total ice thickness (km)*	*Brittle layer thickness (km)*	*Peak normal stress, any azimuth (kPa)*
1	10^{13}	15	5	113.1
2	10^{13}	30	2	158.7
3	10^{13}	30	5	123.9
4	10^{13}	30	10	93.3
5	10^{13}	60	5	146.9
6	10^{13}	**100**	**5**	170.0
7	10^{14}	15	2	103.1
8	10^{14}	15	5	94.4
9	10^{14}	15	10	81.2
10	10^{14}	30	2	81.2
11	10^{14}	**30**	**5**	77.9
12	10^{14}	30	10	71.5
13	10^{14}	60	2	58.6
14	10^{14}	**60**	**5**	57.9
15	10^{14}	60	10	55.9
16	10^{14}	100	5	44.6
17	$\mathbf{10^{15}}$	**15**	**5**	70.5
18	10^{15}	30	2	49.0
19	10^{15}	30	5	49.1
20	10^{15}	30	10	49.4
21	10^{15}	60	5	33.3
22	10^{15}	100	5	24.9

Bold indicated cases shown in Figs. 1–4. Gray indicates cases that do not produce stresses of at least 50 kPa with either eccentricity or period we tested.

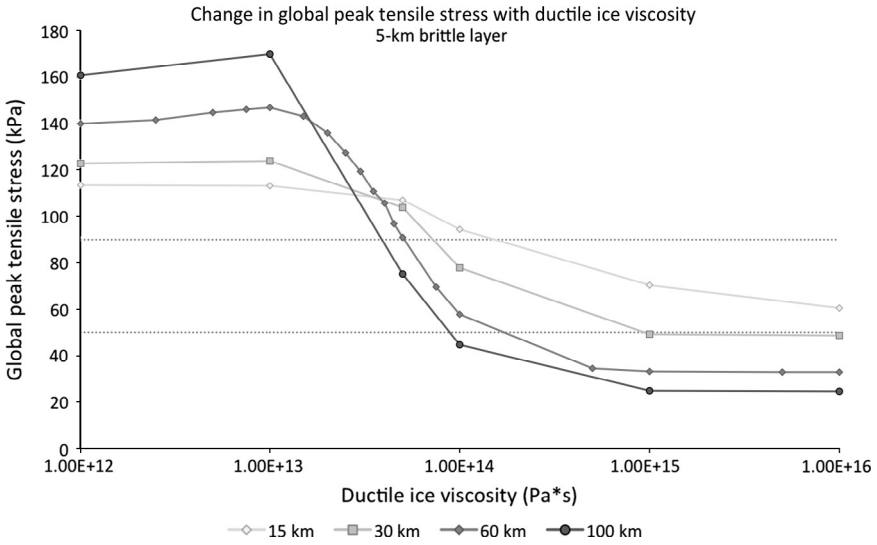

Fig. 1. The variation in global peak tensile stress with viscosity for each value of total ice shell thickness (brittle + ductile). All cases shown here assume a 5-km brittle layer thickness. We have included a wide range of plausible viscosity values to map out the parameter space. In general, the global peak stress increases as the viscosity decreases, with thicker shells experiencing a larger increase than thinner shells. Gray dotted lines bound the range of tensile stresses at which fractures on Europa are thought to have formed. If Charon's ice shell fails under similar conditions, there are many interior structures that would have allowed for the formation of eccentricity-driven fractures.

for each value of the total ice shell thickness, assuming a 5-km thick brittle layer. Global peak tensile stress is a good proxy for the extent of azimuths and locations at which we would predict faulting. In order to characterize the entire plausible parameter space, we have also included viscosity values of 10^{12} and 10^{16} Pa s; the global peak stresses are very similar to those computed for 10^{13} and 10^{15} Pa s, respectively. We also calculated the global peak tensile stress for several intermediate viscosity values, using a 60-km thick total ice shell, to ensure that the trend is well-behaved. For all shell thicknesses, the global peak tensile stress increases as the viscosity of the ductile ice layer decreases (except for a slight turn over between 10^{12} and 10^{13} Pa s for thick shells). The magnitude of the increase depends on the total ice shell thickness.

In Fig. 1, we have added dashed lines at 50 kPa and 90 kPa, which bound the range of tensile failure stresses indicated by fits to Europa's cycloids (Rhoden et al., 2010). By inspection, we can see that our choice of a 50-kPa failure stress would enable at least some faulting for each viscosity value, depending on shell thickness, and for any shell thickness, given a certain viscosity (as described in detail below). In contrast, if the failure stress were 90 kPa, we would only predict faults in cases with a ductile ice viscosity of 10^{13} Pa s or lower and for the moderate viscosity case (10^{14} Pa s) with a 15-km thick total ice shell. With a failure stress of only 20 kPa, as implied by analysis of Europa's lineaments (Rhoden and Hurford, 2013), at least some fractures would form in all cases. It is worth noting that peak compressive stresses are equal in magnitude to the peak tensile stresses. Given that ice fails more easily in tension, we consider it much less likely that eccentricity-driven *compressive* fractures would form on Charon.

Trends in global peak tensile stress with total ice shell thickness and brittle shell thickness are shown in Figs. 2 and 3, respectively, for each viscosity value. For moderate to high viscosity cases (10^{14}–10^{16} Pa s), global peak tensile stress decreases with increasing total ice shell thickness, likely because a thinner shell allows for a correspondingly larger ocean to respond to Pluto's gravitational pull.

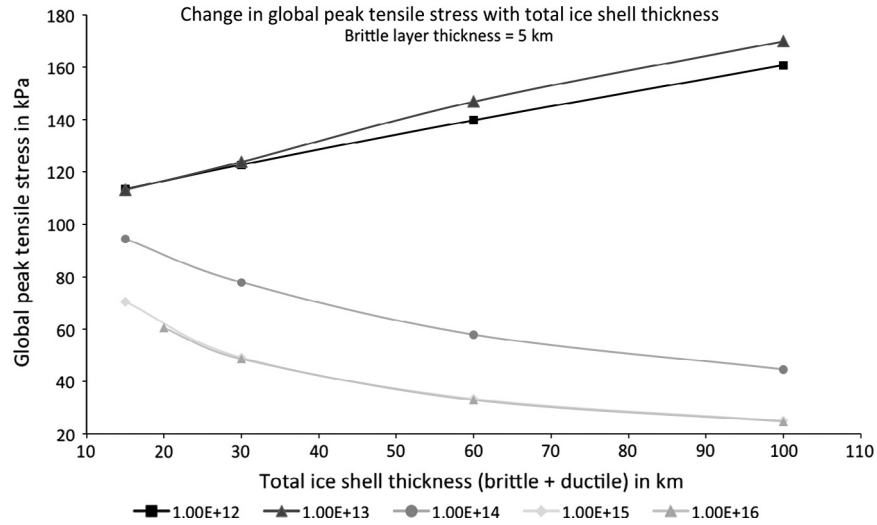

Fig. 2. The variation in global peak tensile stress with total ice shell thickness for each viscosity value. All cases shown here assume a 5-km brittle layer thickness. For the two lowest viscosity values we tested (10^{12} and 10^{13} Pa s), the global peak stress actually increases with ice shell thickness.

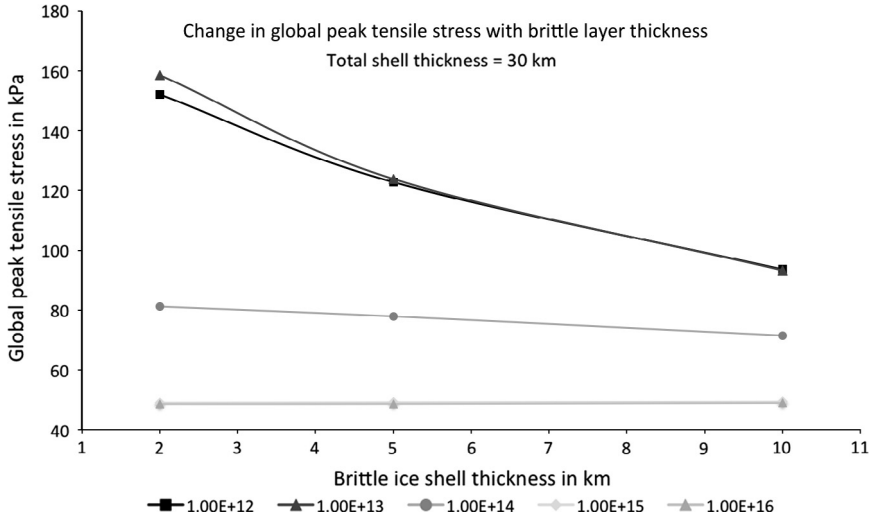

Fig. 3. The variation in peak tensile stress with brittle ice shell thickness for each viscosity value. All cases shown here assume a 30-km total ice shell thickness. For the high viscosity case (10^{15} Pa s), the peak stress is largely insensitive to the brittle shell thickness. In contrast, as the brittle layer thickness is decreased from 10 km to 2 km, the peak stress increases by 14% in the moderate viscosity case (10^{14} Pa s) and 70% in the low viscosity case (10^{13} Pa s).

The opposite trend is observed for viscosities of 10^{12} and 10^{13} Pa s. We hypothesize that the lower viscosities allow the ductile ice layer to respond to tidal forcing more like a fluid than a solid, leading to an enhanced tidal response and higher stress. Global peak tensile stress also increases with decreasing brittle layer thickness, and this trend is much more pronounced in the low viscosity cases (Fig. 3).

The general pattern of eccentricity-driven fractures is well-illustrated by our baseline model (Case 11; Tables 1 and 2), which is shown in Fig. 4. Azimuths at which we would predict faults are shown in gray. The azimuths cluster, creating gray wedges within each latitude/longitude bubble. Along the leading and trailing apexes (90°W and 270°W, respectively), faults are predominantly east–west trending, with the range of allowed azimuths increasing from the equator to the poles. Near the sub-Pluto and anti-Pluto points (0°W and 180°W, respectively) and close to the equator (15°N to 15°S), fractures with nearly any azimuth could form. In contrast, the mid-latitudes (30–60°N, 30–60°S) are more sparsely populated, with no faults predicted at longitudes 0/180°W in this case. Predictions in polar regions vary with longitude and allow a wide range of azimuths. All test cases display this basic pattern, with narrower/fewer wedges for cases that achieve lower stresses and wider/more wedges for cases with higher stresses (global peak tensile stress for each case is listed in Table 2). Hence, further differentiation into specific interior structure models should also be possible, as long as fractures are well-preserved and globally-imaged.

With a viscosity of 10^{15} Pa s, we only predict fracture formation in the case with the thinnest ice shell (Case 17). As shown in Fig. 5, this case would produce a moderate amount of faulting. Although similar to Case 11 (Fig. 4), the extent of faulting near the equator at

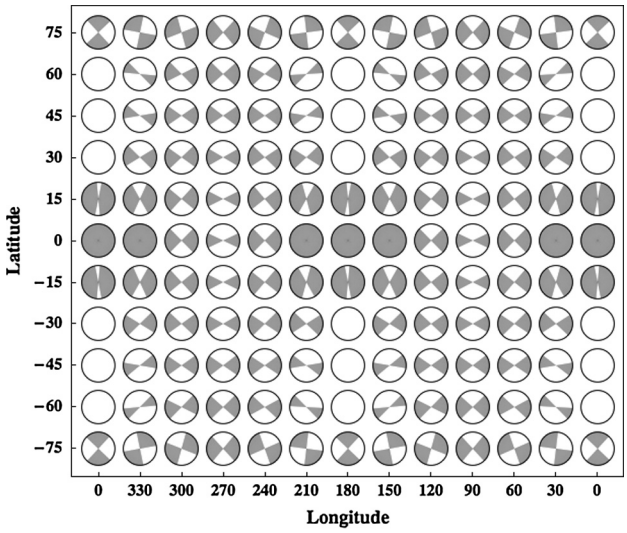

Fig. 4. Azimuths at which tensile fractures are predicted to form are shown in gray, on a latitude–longitude grid, assuming a failure stress of 50 kPa, eccentricity of 0.01, and a period of 3.194 d. In this baseline case (Case 11 in Table 2), the ice shell is 30-km thick, the upper brittle layer is 5-km thick, and the lower ductile layer has a viscosity of 10^{14} Pa s. The general pattern of eccentricity-driven fractures is apparent, with east–west trending fractures along the leading and trailing apexes (longitudes 90°W and 270°W, respectively), and a wider variation in azimuth from equator to pole. Near the sub-Pluto and anti-Pluto points, (longitudes 0°W and 180°W, respectively) more uniform fracture azimuths are predicted near the equator while mid-latitudes would have a sparser population of fractures.

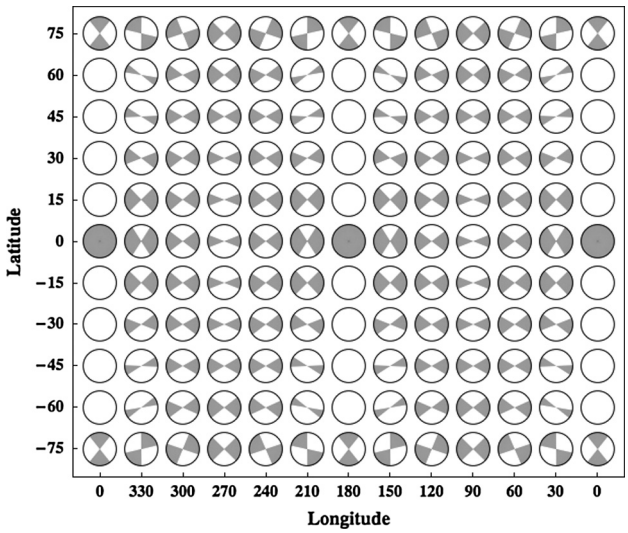

Fig. 5. Azimuths at which tensile fractures are predicted to form are shown in gray, on a latitude–longitude grid, assuming a failure stress of 50 kPa, eccentricity of 0.01, and a period of 3.194 d. This is the only case in which we predict fracture formation using a ductile ice viscosity of 10^{15} Pa s (Case 17), which corresponds to the thinnest shell we tested using this viscosity (15 km, with a 5-km brittle layer).

longitudes 0°W and 180°W is much more limited in this case. Overall, with this viscosity, stress increases with decreasing total ice shell thickness (see Fig. 2). If the tidal stresses were larger (e.g. due to a higher eccentricity) or the failure threshold was much lower, fractures may be allowed with this viscosity, with more fractures predicted for a 30-km ice shell (e.g. Case 19) than a 60-km shell (e.g. Case 21).

Reducing the viscosity to 10^{14} Pa s allows fracturing for a variety of interior models, with thinner ice shells allowing more fractures. Figs. 4 and 6 show the predicted fractures for 30-km (Case 11) and 60-km (Case 14) ice shells, respectively. We assumed a 5-km brittle ice layer in both cases. Predictions for all cases that would produce fractures are shown in the Supplementary Online Material (SOM). The most widespread fracturing is predicted for the thinnest shell, 15 km, with either a 2-km or 5-km thick brittle layer (Cases 7 and 8, respectively). With a 10-km thick brittle layer, we would not predict faults at mid-latitudes at longitudes 0/180°W. Cases with 30-km shells produce similar results, especially with thin brittle layers, so it would be difficult to distinguish between them. With a 60-km shell (Fig. 6), we only predict fractures within 30° of the equator, and the fractures would be oriented east–west. Changing the brittle layer thickness only slightly changes these predictions. We predict no fractures for ice shells 100 km thick.

With the lowest viscosity, 10^{13} Pa s, we predict pervasive fracturing in nearly all cases. Unlike the high and moderate viscosity cases, we find that the pervasiveness of fracturing actually increases with increasing ice shell thickness (see Fig. 1). Furthermore, the increase in predicted faulting from case to case tracks, exactly, a decrease in the ratio of brittle layer thickness to total thickness because a larger proportion of the ice shell is then ductile, low-viscosity ice. This behavior leads to the somewhat counter-intuitive result that the thickest ice shell (100 km, Case 6) produces the highest global peak stress and the most fractures. As shown in Fig. 7, nearly every azimuth could form at latitudes between 30°N and 30°S, and we predict a wide variety of azimuths, depending on longitude, poleward of 60°. We still predict limited north–south oriented faults at mid-latitudes and along the leading and trailing apexes (90°W and 270°W, respectively). If such pervasive fracturing were observed on Charon, it may be difficult to further constrain the properties of the ice shell because the predicted fracture patterns are so similar (predictions for all cases are shown in the SOM). In particular, varying the brittle layer thickness can make the predicted fracture patterns for thick (e.g. 100 km in Case 6) and thin (e.g. 30 km in Case 2) ice shells so similar that only an idealized population of faults could differentiate between the two.

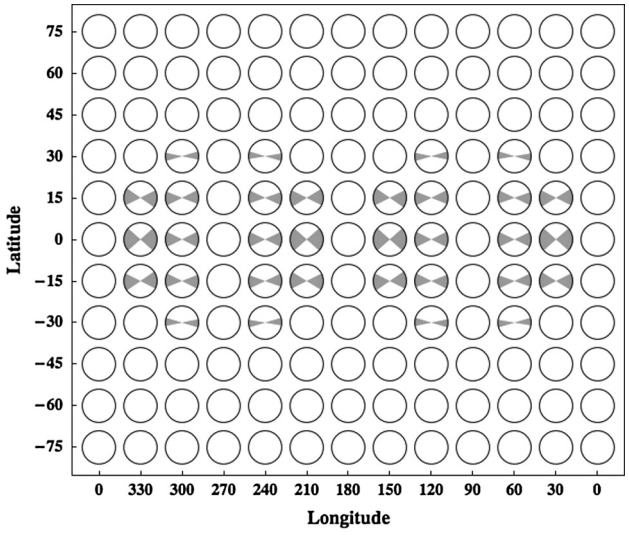

Fig. 6. Azimuths at which tensile fractures are predicted to form are shown in gray, on a latitude–longitude grid, assuming a failure stress of 50 kPa, eccentricity of 0.01, and a period of 3.194 d. In this case, the ice shell is 60-km thick, the upper brittle layer is 5-km thick, and the lower ductile layer has a viscosity of 10^{14} Pa s (Case 14 in Table 2). The thicker ice shell vastly reduces the locations at which we would predict fault formation, as compared with a 30-km shell (Case 11, Fig. 4). Only the east–west trending fractures near the leading and trailing apexes are preserved. Hence, the tectonic record should provide constraints on Charon's ice shell thickness at the time of fracture formation.

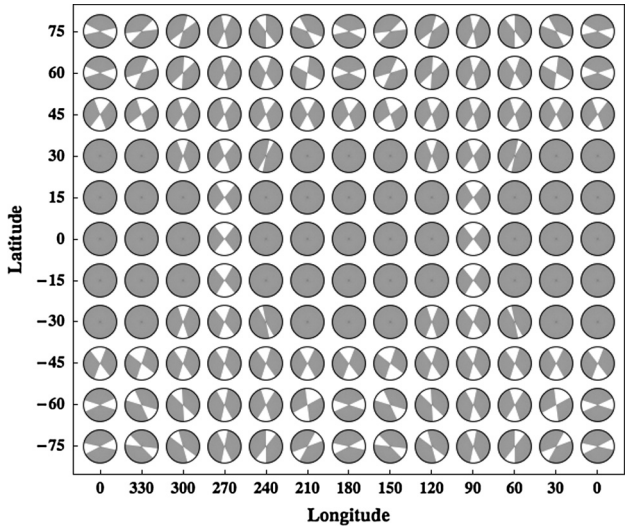

Fig. 7. Azimuths at which tensile fractures are predicted to form are shown in gray, on a latitude–longitude grid, assuming a failure stress of 50 kPa, eccentricity of 0.01, and a period of 3.194 d. This case (Case 6 in Table 2) produces fractures at nearly all azimuths in most locations. Assuming a low viscosity of 10^{13} Pa s for the ductile ice layer results in the thickest shell (100 km) producing the highest stresses and the most pervasive fracturing. If such fracturing were observed on Charon, it would be a strong indication that Charon experienced a period of high eccentricity and remained warm as its orbit evolved.

5. Discussion

Given the predictions described in the previous section, the overall extent of fracturing should enable us to constrain the viscosity of the ice shell, with more extensive fracturing implying a warmer, less viscous shell. Variations in the observed pattern of fracturing may further enable us to constrain the thickness of the ice shell and its component layers. For example, the distributions of azimuths along the sub-Pluto and anti-Pluto points (0°W and 180°W, respectively) are particularly diagnostic. If fractures are observed in most regions, but only limited fracturing occurred at longitudes 0/180°W, it would indicate a 30-km shell with moderate viscosity (e.g. Case 11, Fig. 4). Whereas, a wide variety of fault azimuths in these regions would imply a lower viscosity (e.g. Case 3) or a thinner shell (e.g. Case 8). An extensively fractured surface would be strongly suggestive of a low viscosity ductile ice layer, but in that case, the total thickness of the ice shell may be left largely unconstrained.

The failure stress we assume affects our constraint on Charon's period at the time of high eccentricity and fracture formation. As described above, we would not predict any faults to form at the current period using a failure stress of 50 kPa. In the case that produces the highest stresses (Case 6), even a failure stress of 40 kPa would barely allow fractures to form. However, a failure stress of 20 kPa would allow moderate faulting in most cases with low viscosity (10^{13} Pa s) and some faulting in cases with a moderate viscosity (10^{14} Pa s) for shells 30 km or thinner. Hence, fractures could have formed on Charon at or very near its current period if the failure stress was closer to 20 kPa (rather than 50 kPa) or the

eccentricity were higher than 0.01 at that time. Even a 20% higher eccentricity would allow faults to form at a failure stress of 50 kPa in at least some cases. In fact, orbital evolution models suggest that Charon's eccentricity could be as high as 0.1–0.3, even in the end stages of Charon's orbital recession (Cheng et al., 2014), which would lead to large enough stresses to exceed our 50-kPa failure threshold even with a high viscosity (10^{15} Pa s) and a thick shell.

The ambiguity in eccentricity, period, and ice strength somewhat limits the diagnostic power of tectonic features that may be preserved on Charon's surface. However, the pattern predicted for eccentricity-driven faulting remains unchanged in these different scenarios, as do the trends in faulting as interior structure parameters are varied (e.g. an increase in pervasiveness of faulting with decreasing ductile ice viscosity). Hence, we should be able to use Charon's tectonic record to draw some general conclusions. First, the presence of fractures at and around the sub-Pluto and anti-Pluto points (0°W, 180°W) would strongly suggest that eccentricity-driven fractures formed at some point in Charon's past. If no such fractures are observed, we would conclude that either Charon's eccentricity remained low (likely <0.001), the failure threshold was greater than that implied at Europa, or Charon's interior was cool enough to preserve a rather thick ice shell and keep the ductile ice layer highly viscous. On the other hand, if Charon's surface displays a moderate to large number of fractures that exhibit the characteristic pattern of eccentricity-driven tidal stress, it would suggest that Charon's eccentricity was greater than 0.001, and likely 0.01 or larger, before reaching its present orbital position and that the viscosity of Charon's lower, ductile ice shell was no more than 10^{14} Pa s when the fractures formed. More detailed analysis of observed fractures may also enable us to constrain the thickness and viscosity of the ice shell for a range of failure stress assumptions.

Tensile fractures may also have formed on Charon in response to tidal stress from despinning or orbital recession, in addition to the eccentricity-driven fractures we predict. For example, despinning stresses would produce strictly east–west fractures (180° azimuth) near the equator and at mid-latitudes (e.g. Melosh, 1977; Kattenhorn and Hurford, 2009). Poleward of 50°N and 50°S, strictly north–south fractures (90° azimuth) could also form. Furthermore, the fracture predictions from despinning are uniform in longitude, and stresses are higher at the poles than at the equator, so more fracturing would be expected at high latitudes. This is quite different from the general pattern we find for eccentricity-driven tensile fractures (see Fig. 4 and Section 4), which is longitude-dependent, would produce nearly all azimuths in at least some equatorial regions, and would allow N–S fractures in very limited locations. Even in the case that produces the most fractures (Case 6, Fig. 7), there are regions where N–S fractures would not form. Finally, any fractures formed from despinning stresses should be among the oldest features in the geologic record and would certainly predate eccentricity-driven fractures.

On the other hand, Charon's orbital recession would have occurred concurrently with the eccentricity evolution, so any resulting fractures may overlap within the geologic record. However, there are distinct differences between the patterns of stress from these two sources, such that careful analysis could distinguish between them. In particular, stress caused by Charon's orbital recession would generate solely compressive stress at the sub-Pluto and anti-Pluto points (e.g. Kattenhorn and Hurford, 2009; see also Barr and Collins, 2013). Hence, we would not expect tensile fractures to form at those longitudes. In contrast, tensile fractures that form in response to eccentricity-driven tidal stress (e.g. Figs. 4 and 7) could produce fractures in these regions. Therefore, it should be possible to distinguish eccentricity-driven fractures from those generated by despinning and/or orbital recession stresses based on global mapping, stratigraphy, and statistical analysis (e.g. Rhoden and Hurford, 2013).

The penetration depth of fractures on icy satellites is not well constrained. Downward propagation of fractures should be limited by the magnitude of the overburden stress (ρgh) – a compressive stress that competes with the tensile stress due to tides – and by stress relaxation in ductile ice. Both of these effects will be enhanced with increasing depth within the shell because the overburden stress is higher and the ice is warmer. On Europa, the overburden stress should equal the tensile stress implied by cycloid fits (50–90 kPa) at a depth of only 40–70 m. On Enceladus, the depth would be 440 m, and on Charon, it would be 180 m. However, fractures may be able to penetrate significantly deeper than the overburden closure depth on both Europa and Enceladus. Rudolph and Manga (2009) found that 1-MPa tensile stresses, which would correspond to a ~9 km overburden closure depth, could fracture completely through an Enceladean ice shell up to 25-km thick. Charon's surface gravity is about 2.5 times that of Enceladus, which would imply a lower fracture penetration depth. However, if tidal fractures are observed on Charon, it seems plausible that they penetrate through the entire brittle ice layer, which may have allowed for past cryovolcanic activity.

For the purposes of this work, we have selected combinations of orbital parameters and interior structure models that represent snapshots in time during Charon's hypothetical evolution. When the New Horizons spacecraft arrives at Charon, and provides the imaging data set critical to this work, these predictions will allow us to begin to constrain Charon's past eccentricity and interior structure. Furthermore, detailed analysis of eccentricity-driven fractures on Charon may enable a more sophisticated time-varying study, using a fully-coupled thermal–orbital evolution model, with implications for the formation and evolution of the entire Pluto–Charon system.

The differences between our predicted fracture patterns demonstrate that the tectonic record of a body that has experienced tidal deformation may be used to constrain its interior. Hence, the techniques we have developed are widely applicable. Saturnian satellites, Dione and Rhea, and Neptune's Triton, may also have possessed subsurface oceans and undergone tidal deformation. By comparing fractures observed on each of these satellites with tidal-tectonic predictions, analogous to those we have shown here for Charon, we could determine whether the fractures correspond to tidal stress patterns, the minimum ocean thickness required to have generated the necessary tidal stress, and the rheology of the ice shell. Therefore, this approach can provide insight as to the extent of tidal-tectonic processes and habitable environments within our Solar System.

6. Conclusions

The New Horizons spacecraft should provide the first images of the surfaces of Pluto and Charon. Our predictions indicate that the presence (or absence) of tidally-driven fractures could be used to constrain Charon's internal structure and orbital parameters at the time of fracture formation. Furthermore, these fractures should be distinct from those produced through orbital recession and despinning. If tidally-driven fractures are quite prevalent, it would require that Charon experienced a high eccentricity during its orbital evolution and that the ice shell remained relatively warm during this time period. In contrast, very limited tidal fracturing would place upper limits on Charon's eccentricity and the viscosity of the ice shell. The specific distribution of fractures, either sparse or numerous, could be used to further distinguish between a thick and thin ice shell.

If Charon is tidally-active today, a source other than eccentricity must be driving tidal deformation. Fractures on Europa display characteristics that are best explained through the addition of a

non-zero obliquity (e.g. Rhoden et al., 2010) into tidal stress calculations. Europa's non-zero obliquity has now been confirmed through Earth-based radar observations (Margot et al., 2013). However, unlike at Jupiter, there are no other large satellites at Pluto that could force Charon's obliquity, and we would expect the obliquity to have damped out long ago. Nevertheless, if Charon's obliquity was non-zero during a tidally-active phase, the asymmetric stress pattern diagnostic of obliquity should be recorded in fracture patterns (e.g. Rhoden and Hurford, 2013).

Once we have obtained surface images, mapping and modeling of tidally-driven fractures will enable more sophisticated assessments of Charon's coupled thermal–orbital evolution as well as investigations into addition tidal stress contributions, such as those from a non-zero obliquity. Hence, the images obtained by the New Horizons spacecraft would vastly improve our understanding of the formation and evolution of the entire Pluto–Charon system.

Acknowledgments

The authors wish to thank H. Jara-Orué and B. Vermeersen for their assistance with development of the tidal response code and G. Collins for thoughtful discussions that led to this manuscript. A. Rhoden and W. Henning were partially supported through appointments to the NASA Postdoctoral Program at the NASA Goddard Space Flight Center, administered by Oak Ridge Associated Universities.

Appendix A

Following the propagator matrix method (Love, 1927; Alterman et al., 1959; Takeuchi et al., 1962; Peltier, 1974; Sabadini and Vermeersen, 2004), as described in detail by Jara-Orué and Vermeersen (2011), we compute the loading response of a series of laterally homogeneous incompressible material layers within the Laplace domain. We specify a shear modulus, viscosity, and density for each layer (see Table 1) and compute the response across a broad range of timescales. Results from this calculation include the frequency of the normal modes of free oscillation for Charon, the relative strengths of each normal mode, and the elastic surface displacement Love numbers for the spherical harmonic degree 2 tidal component of Charon's tidal deformation. While higher degree spherical harmonic components may play a role for Charon, due to the proximity and relative size of Pluto, only degree two terms are considered for this work as an initial assessment of Charon's behavior.

For our assumed structure, with a single unstratified water ocean layer, there are six normal modes of free oscillation in the solution, characterized by the terms s_j (where $j = 1, \ldots, 6$) or by the periods, s_j (where $s_j = -1/s_j$). Note that all normal modes, s_j, are negative values, and all s values are positive. An advantage of using the normal mode method (i.e. Laplace domain method) for the tidal response calculation is its applicability to aperiodic forcing conditions, in contrast with the Fourier-domain approach for periodic forcing. The specific formulation that we have adapted from Jara-Orué and Vermeersen (2011) assumes an inviscid core. We have found this assumption to have minimal impact upon results for Charon; rather, the ice shell structure largely controls the tidal response. We find that an inviscid core is functionally equivalent to a low viscosity core in the appropriate range for iron (Frost and Ashby, 1982).

We have verified our implementation of the approach presented by Jara-Orué and Vermeersen (2011) in three ways. First, we have reproduced the results of Jara-Orué and Vermeersen (2011) for Europa to less than 1% error. Second, we have compared our results to a range of cases dominated by solid-only layers (Sabadini and Vermeersen, 2004), and found general agreement. Lastly, we have obtained the same surface Love numbers using the TideLab code suite, provided by William Moore, which uses a robust, alternative methodology for assessing multiple layers, including true liquid interfaces (Wolf, 1994; Moore and Schubert, 2000).

An exploration of viscoelastic behavior for Charon is especially important because the ~6 day orbital period is close to the optimal tidal coupling frequency (e.g. the Maxwell time) for ice, leading the system to be very sensitive to small changes in ice viscosity. We assume a Maxwell rheology throughout this work (Henning et al., 2009), while recognizing that other rheologies, such as the Andrade or Burgers models may be useful for future investigations (Burgers, 1935; Karato and Spetzler, 1990; Efroimsky, 2012). For simplicity, we do not attempt to link our assumed ice viscosities with specific ice impurities, clathrates, or mixtures (e.g. Hogenboom et al., 1997; Kargel, 1998; Eluszkiewicz and Stevenson, 1990). However, in general, lower viscosities and shear moduli are consistent with higher impurity concentrations.

Appendix B. Supplementary material

Supplementary data associated with this article can be found, in the online version, at http://dx.doi.org/10.1016/j.icarus.2014.04.030.

References

Alterman, Z., Jarosch, H., Pekeris, C.L., 1959. Oscillations of the Earth. Proc. R. Soc. Lond. Ser. A: Math. Phys. Sci. 252 (1268), 80–95.
Anderson, J.D., Schubert, G., Jacobson, R.A., Lau, E.L., Moore, W.B., Sjogren, W.L., 1998. Europa's differentiated internal structure: Inferences from four Galileo encounters. Science 281, 2019–2022.
Barr, A.C., Collins, G.C., 2013. Despinning and tidally driven tectonics in the Pluto–Charon binary system. American Geophysical Union (Fall). Abstract P44A-08.
Behounková, M., Tobie, G., Choblet, G., Cadek, O., 2012. Tidally-induced melting events as the origin of south-pole activity on Enceladus. Icarus 219, 655–664.
Brown, M.E., 2002. Pluto and Charon: Formation, seasons, composition. Annu. Rev. Earth Planet. Sci. 30 (1), 307–345.
Brown, M.E., Calvin, W.M., 2000. Evidence for crystalline water and ammonia ices on Pluto's satellite Charon. Science 287 (5450), 107–109.
Buie, M.W., Grundy, W.M., 2000. The distribution and physical state of H_2O on Charon. Icarus 148 (2), 324–339.
Buie, M.W., Tholen, D.J., Wasserman, L.H., 1997. Separate lightcurves of Pluto and Charon. Icarus 125 (2), 233–244.
Buie, M.W., Grundy, W.M., Young, E.F., Young, L.A., Stern, S.A., 2006. Orbits and photometry of Pluto's satellites: Charon, S/2005 P1, and S/2005 P2. Astron. J. 132 (1), 290–298.
Buie, M.W., Tholen, D.J., Grundy, W.M., 2012. The orbit of Charon is circular. Astron. J. 144 (1), 15–34.
Burgers, J.M., 1935. Mechanical considerations, model systems, phenomenological theories of relaxation and of viscosity. In: Burgers, J.M. (Ed.), First Report on Viscosity and Plasticity, vol. 1. Nordemann Publishing Company, New York.
Canup, R.M., 2005. A giant impact origin of Pluto–Charon. Science 307 (5709), 546–550.
Cheng, W.H., Lee, M.H., Peale, S.J., 2014. Complete tidal evolution of Pluto-Charon. Icarus 233, 242–258.
Collins, G.C., Goodman, J.C., 2007. Enceladus' south polar sea. Icarus 189, 72–82.
Cook, J.C., Desch, S.J., Roush, T.L., Trujillo, C.A., Geballe, T.R., 2007. Near-infrared spectroscopy of Charon: Possible evidence for cryovolcanism on Kuiper belt objects. Astrophys. J. 663 (2), 1406–1419.
Cruikshank, D.P. et al., 1997. The surfaces of Pluto and Charon. Pluto Charon 1, 221–267.
Desch, S.J., Cook, J.C., Doggett, T.C., Porter, S.B., 2009. Thermal evolution of Kuiper belt objects, with implications for cryovolcanism. Icarus 202 (2), 694–714.
Efroimsky, M., 2012. Tidal dissipation compared to seismic dissipation: In small bodies, Earths, and super-Earths. Astrophys. J. 746 (2), 150–170.
Eluszkiewicz, J., Stevenson, D.J., 1990. Rheology of solid methane and nitrogen: Applications to Triton. Geophys. Res. Lett. 17 (10), 1753–1756.
Figueredo, P.H., Greeley, R., 2000. Geologic mapping of the northern leading hemisphere of Europa from Galileo solid-state imaging data. J. Geophys. Res. 105, 22629–22646.
Fountain, G.H. et al., 2009. The new horizons spacecraft. In: New Horizons. Springer, New York, pp. 23–47.
Frost, H.J., Ashby, M.F., 1982. Deformation Mechanism Maps: The Plasticity and Creep of Metals and Ceramics. Pergamon Press, New York.
Geissler, P.E. et al., 1998. Evolution of lineaments on Europa: Clues from Galileo multispectral imaging observations. Icarus 135, 107–126.

Goldreich, P.M., Mitchell, J.L., 2010. Elastic shells of synchronously rotating moons: Implications for cracks on Europa and non-synchronous rotation on Titan. Icarus 209, 631–638.
Goldsby, D.L., Kohlstedt, D.L., 2001. Superplastic deformation of ice: Experimental observations. J. Geophys. Res.: Solid Earth (1978–2012) 106 (B6), 11017–11030.
Greenberg, R., Geissler, P., Hoppa, G., Tufts, B.R., Durda, D.D., Pappalardo, R., et al., 1998. Tectonic processes on Europa: Tidal stresses, mechanical response, and visible features. Icarus 135 (1), 64–78.
Groenleer, J., Kattenhorn, S.A., 2008. Cycloid crack sequences on Europa: Relationship to stress history and constraints on growth mechanics based on cusp angles. Icarus 193, 158–181.
Hedman, M.M. et al., 2013. An observed correlation between plume activity and tidal stresses on Enceladus. Nature 500 (7461), 182–184.
Helfenstein, P., Parmentier, E.M., 1983. Patterns of fracture and tidal stresses on Europa. Icarus 53, 415–430.
Helfenstein, P., Parmentier, E.M., 1985. Patterns of fracture and tidal stresses due to nonsynchronous rotation – Implications for fracturing on Europa. Icarus 61, 175–184.
Henning, W.G., O'Connell, R.J., Sasselov, D.D., 2009. Tidally heated terrestrial exoplanets: Viscoelastic response models. Astrophys. J. 707 (2), 1000–1015.
Hogenboom, D.L., Kargel, J.S., Consolmagno, G.J., Holden, T.C., Lee, L., Buyyounouski, M., 1997. The ammonia–water system and the chemical differentiation of icy satellites. Icarus 128 (1), 171–180.
Hoppa, G.V., Tufts, B.R., Greenberg, R., Hurford, T.A., O'Brien, D.P., Geissler, P.E., 2001. Europa's rate of rotation derived from the tectonic sequence in the Astypalaea region. Icarus 153, 208–213.
Hurford, T.A., Helfenstein, P., Hoppa, G.V., Greenberg, R., Bills, B.G., 2007a. Eruptions arising from tidally controlled periodic openings of rifts on Enceladus. Nature 447 (7142), 292–294.
Hurford, T.A., Sarid, A.R., Greenberg, R., 2007b. Cycloidal cracks on Europa: Improved modeling and non-synchronous rotation implications. Icarus 186 (1), 218–233.
Hurford, T.A., Helfenstein, P., Spitale, J.N., 2012. Tidal control of jet eruptions on Enceladus as observed by Cassini ISS between 2005 and 2007. Icarus 220 (2), 896–903.
Iess, L. et al., 2014. Science 344, 78–80.
Jara-Orué, H.M., Vermeersen, B.L., 2011. Effects of low-viscous layers and a non-zero obliquity on surface stresses induced by diurnal tides and non-synchronous rotation: The case of Europa. Icarus 215 (1), 417–438.
Karato, S.I., Spetzler, H.A., 1990. Defect microdynamics in minerals and solid-state mechanisms of seismic wave attenuation and velocity dispersion in the mantle. Rev. Geophys. 28 (4), 399–421.
Kargel, J.S., 1998. Physical chemistry of ices in the outer Solar System. In: Solar System Ices. Springer, Netherlands, pp. 3–32.
Kattenhorn, S.A., 2002. Nonsynchronous rotation evidence and fracture history in the Bright Plains region, Europa. Icarus 157, 490–506.
Kattenhorn, S.A., Hurford, T., 2009. Tectonics of Europa. In: Europa, The University of Arizona Space Science Series. University of Arizona Press, Tucson, pp. 199–236.
Lee, M.H., Peale, S.J., 2006. On the orbits and masses of the satellites of the Pluto–Charon system. Icarus 184 (2), 573–583.
Litwin, K.L., Zygielbaum, B.R., Polito, P.J., Sklar, L.S., Collins, G.C., 2012. Influence of temperature, composition, and grain size on the tensile failure of water ice: Implications for erosion on Titan. J. Geophys. Res.: Planets 117, 1991–2112.
Love, A.E., 1927. A Treatise on the Mathematical Theory of Elasticity. Cambridge Univ. Press, Cambridge, UK.
Margot, J.-L., Padovan, S., Campbell, D., Peale, S., Ghigo, F., 2013. Measurements of the Spin States of Europa and Ganymede. American Astronomical Society, DPS Meeting #45, Abstract #504.02.
McKinnon, W.B., 1989. On the origin of the Pluto–Charon binary. Astrophys. J. 344, L41–L44.
Melosh, H.J., 1977. Global tectonics of a despun planet. Icarus 31, 221–243.
Moore, W.B., Schubert, G., 2000. The tidal response of Europa. Icarus 147 (1), 317–319.
Nesvorný, D., Youdin, A.N., Richardson, D.C., 2010. Formation of Kuiper belt binaries by gravitational collapse. Astron. J. 140 (3), 785–793.
Nimmo, F., 2004. Stresses generated in cooling viscoelastic ice shells: Application to Europa. J. Geophys. Res.: Planets 109. http://dx.doi.org/10.1029/2004JE002347.
Nimmo, F., Spencer, J.R., Pappalardo, R.T., Mullen, M.E., 2007. Shear heating as the origin of the plumes and heat flux on Enceladus. Nature 447, 289–291.
Null, G.W., Owen, W.M., Synnott, S.P., 1993. Masses and densities of Pluto and Charon. Astron. J. 105, 2319–2335.
Patthoff, D., Kattenhorn, S., 2011. A fracture history on Enceladus provides evidence for a global ocean. Geophys. Res. Lett. 38 (18). http://dx.doi.org/10.1029/2011GL048387.
Peale, S.J., 1999. Origin and evolution of the natural satellites. Annu. Rev. Astron. Astrophys. 37, 533–602.
Peltier, W.R., 1974. The impulse response of a Maxwell Earth. Rev. Geophys. Space Phys. 12, 649–669.
Piros dos Santos, P.M., Morbidelli, A., Nesvorný, D., 2012. Dynamical capture in the Pluto–Charon system. Celest. Mech. Dyn. Astron. 114 (4), 341–352.
Poirier, J.P., 1982. Rheology of ices: A key to the tectonics of the ice moons of Jupiter and Saturn. Nature 299, 683–687.
Porco, C.C. et al., 2006. Cassini observes the active south pole of Enceladus. Science 311 (5766), 1393–1401.
Protopapa, S. et al., 2008. Surface characterization of Pluto and Charon by L and M band spectra. Astron. Astrophys. 490 (1), 365–375.
Rhoden, A.R., Hurford, T.A., 2013. Lineament azimuths on Europa: Implications for obliquity and non-synchronous rotation. Icarus 226 (1), 841–859.
Rhoden, A.R., Militzer, B., Huff, E.M., Hurford, T.A., Manga, M., Richards, M.A., 2010. Constraints on Europa's rotational dynamics from modeling of tidally-driven fractures. Icarus 210 (2), 770–784.
Rhoden, A.R., Wurman, G., Huff, E.M., Manga, M., Hurford, T.A., 2012. Shell tectonics: A mechanical model for strike-slip displacement on Europa. Icarus 218, 297–307.
Rhoden, A.R., Jara-Orué, H., Hurford, T., Vermeersen, B., 2013. Cycloid Formation in Europa's Viscoelastic Ice Shell. American Astronomical Society, DPS Meeting #45, Abstract #504.01.
Roberts, J.H., Nimmo, F., 2008. Tidal heating and the long-term stability of a subsurface ocean on Enceladus. Icarus 194, 675–689.
Roth, L. et al., 2013. Transient water vapor at Europa's south pole. Science. http://dx.doi.org/10.1126/science.1247051.
Rudolph, M., Manga, M., 2009. Fracture penetration in planetary ice shells. Icarus 199 (2), 536–541.
Sabadini, R., Vermeersen, B., 2004. Global Dynamics of the Earth: Applications of Normal Mode Relaxation Theory to Solid-Earth Geophysics, vol. 20. Springer.
Sarid, A.R., Greenberg, R., Hoppa, G.V., Geissler, P., Preblich, B., 2004. Crack azimuths on Europa: Time sequence in the southern leading face. Icarus 168, 144–157.
Sarid, A.R., Greenberg, R., Hoppa, G.V., Brown Jr., D.M., Geissler, P., 2005. Crack azimuths on Europa: The G1 lineament sequence revisited. Icarus 173, 469–479.
Sarid, A.R., Greenberg, R., Hurford, T.A., 2006. Crack azimuths on Europa: Sequencing of the northern leading hemisphere. J. Geophys. Res. 111, E08004. http://dx.doi.org/10.1029/2005JE002524.
Schulson, E.M., 2001. Brittle failure of ice. Eng. Fract. Mech. 68, 1839–1887.
Sicardy, B. et al., 2006. Charon's size and an upper limit on its atmosphere from a stellar occultation. Nature 439 (7072), 52–54.
Spencer, J.R. et al., 2006. Cassini encounters Enceladus: Background and the discovery of a south polar hot spot. Science 311, 1401–1405.
Stern, A., Spencer, J., 2003. New Horizons: The first reconnaissance mission to bodies in the Kuiper belt. Earth, Moon, Planets 92 (1–4), 477–482.
Stern, S.A. et al., 2006. A giant impact origin for Pluto's small moons and satellite multiplicity in the Kuiper belt. Nature 439 (7079), 946–948.
Takeuchi, H., Saito, M., Kobayashi, N., 1962. Statical deformations and free oscillations of a model Earth. J. Geophys. Res. 67 (3), 1141–1154.
Tobie, G., Cadek, O., Sotin, C., 2008. Solid tidal friction above a liquid water reservoir as the origin of the south pole hotspot on Enceladus. Icarus 196, 642–652.
Wahr, J., Selvans, Z.A., Mullen, M.E., Barr, A.C., Collins, G.C., Selvans, M., Pappalardo, R.T., 2009. Modeling stresses on satellites due to nonsynchronous rotation and orbital eccentricity using gravitational potential theory. Icarus 200, 188–206.
Ward, W.R., Canup, R.M., 2006. Forced resonant migration of Pluto's outer satellites by Charon. Science 313 (5790), 1107–1109.
Wolf, D., 1994. Lamé's problem of gravitational viscoelasticity: The isochemical, incompressible planet. Geophys. J. Int. 116 (2), 321–348.
Young, L.A. et al., 2008. New Horizons: Anticipated scientific investigations at the Pluto system. Space Sci. Rev. 140, 93–127.